Brain Structure and Function

Supplementary material to:

Structure-function relationships during segregated and integrated network states of human brain functional connectivity

Makoto Fukushima, Richard F. Betzel, Ye He, Martijn P. van den Heuvel, Xi-Nian Zuo, Olaf Sporns

Corresponding author: Makoto Fukushima, Department of Psychological and Brain Sciences, Indiana University, 1101 East 10th Street, Bloomington, Indiana 47405, USA, *Email address:* mfukushi@indiana.edu

Supplementary methods

Replication dataset

To confirm the reproducibility of results, we employed an independent set of imaging data from Release 1–5 of the enhanced NKI-Rockland Sample. From the NKI dataset, structural networks were newly constructed for the analysis of reproducibility in this study, whereas time-resolved functional networks were derived from a previous study (Betzel et al. 2016). The manners of data preprocessing and network construction in the NKI dataset were different from those adopted in the HCP dataset as described later.

Subject cohort. Imaging data were collected with the approval of the institutional review board and with written informed consent provided by all participants (Nooner et al. 2012). The original number of subjects was 418 over the life-span. By applying a procedure explained in Betzel et al. (2016), we extracted a quality-controlled sub-sample of healthy adults aged $\geq$ 18 and $\leq$ 30 years, comprising 80 participants (42 males and 38 females). Within this sample, DWI data were available in 73 individuals (37 males and 36 females).

Image acquisition. Multimodal MRI data were acquired with a 32-channel head coil on a 3T Siemens Tim Trio scanner. We selected rs-fMRI data with the shortest TR of 645 ms in the NKI dataset to take advantage of the fast sampling to track fluctuations in functional connectivity. The rs-fMRI data were collected with an eyes open condition in a single run of about 10 min (900 time points). Scanning parameters of rs-fMRI data were TE = 30 ms, flip angle = 60°, FOV = 222 × 222 mm^2, 40 slices and voxel size = 3 mm isotropic. DWI data were collected with TR = 2,400 ms, TE = 85 ms, flip angle = 90°, FOV = 212 × 212 mm^2, 64 slices and voxel size = 2 mm isotropic. The total number of DWI volumes was 137, which included 128 volumes with a *b*-value of 1,500 s/mm^2 with different gradient directions and 9 interleaved *b*0 images.

Scanning parameters of a T1-weighted structural image were TR = 1,900 ms, TE = 2.52 ms, flip angle = 9°, FOV = 250 × 250 mm^2, 176 slices and voxel size = 1 mm isotropic.

Preprocessing

As explained in Betzel et al. (2016), the rs-fMRI data were preprocessed with the Connectome Computation System pipeline (Xu et al. 2015), which incorporates functions in standard neuroimaging software: AFNI (Cox 2012), Freesurfer (Fischl 2012), FSL (Jenkinson et al. 2012) and SPM (Ashburner 2012). The rs-fMRI data preprocessing included the following: 1) elimination of the first volumes of 10 s, 2) outlier volume removal and interpolation (the percentage of interpolated volumes was $5.9 \pm 0.5\%$ [mean $\pm$ SD]), 3) slice timing and motion correction, 4) global mean intensity normalization, 5) co-registration between structural and functional images, 6) nuisance regression using the Friston-24 motion time series (Friston et al. 1996) and global, white matter and CSF mean signals, 7) band-pass filtering (0.01–0.1 Hz), 8) linear and quadratic detrending and 9) projection to standard volumetric (MNI152) and surface (fsaverage5) spaces. The low-cut frequency in the band-pass filtering was specified as the reciprocal of the width of the time window for estimating time-resolved functional connectivity (100 s, as described in the following section).

The DWI data were newly preprocessed for this study as follows: 1) realignment, and correction for eddy current and susceptibility distortions, 2) bias field removal using the mean $b0$ image, 3) co-registration between structural and diffusion images, 4) reconstruction of the voxel-wise fiber orientation distribution (FOD) using constrained spherical deconvolution (Tournier et al. 2007) and 5) whole-brain deterministic streamline tractography. FOD reconstruction and streamline tractography were performed using MRtrix (Tournier et al. 2012), allowing for the reconstruction of crossing fiber configurations. The voxel-wise FOD was reconstructed with eight-dimensional spherical harmonics for the response function. A streamline was started 10^6 times randomly in white matter voxels, following FOD peak orientations until a streamline reached the gray matter, exited the brain tissue, made a turn of more than 45° or reached a voxel with either a low FOD amplitude (< 0.1) or a low fractional anisotropy (< 0.1). The number of streamlines interconnecting regions i and j was obtained by counting the number of the reconstructed streamlines that touched both regions i and j.

Network construction

As illustrated in Betzel et al. (2016), networks in the NKI dataset were constructed based on a parcellation used in Betzel et al. (2014) and Yeo et al. (2015) in which the whole cortex was separated into 114 regions, forming a subdivision of the 17 network components in Yeo et al. (2011) (see Fig. S6). One region in the dorsal prefrontal cortex in the left hemisphere was discarded due to its small surface area and the remaining 113 regions were used as nodes for network analysis.

Structural connectivity was quantified using the number of streamlines and the surface area of region in the same manner as in the HCP dataset. Since DWI data were acquired only from a subset of subjects, group-level structural connectivity was used for the assessment of structure-function relationships in the NKI dataset.

Adopted window parameters for the estimation of time-resolved functional connectivity were different from the ones applied to the HCP dataset, as seen in Betzel et al. (2016). In the NKI dataset an exponential tapered window employed in Zalesky et al. (2014) was used to estimate time-resolved functional connectivity with a window width of 100 s, a step size of 1 TR $= 0.645$ s, resulting in a total number of 730 windows. Details of the shape of the tapered window are described in Zalesky et al. (2014) and Betzel et al. (2016).

Supplementary results

Reproducibility of patterns in segregated and integrated states

We confirmed that the patterns in the joint distributions of the within-module degree z-score and the participation coefficient were highly reproducible in each network state across all runs of the HCP and NKI datasets. In all the cases the peak of distributions in the segregated state was at near 0 and the peak in the integrated state was at near 0.5 along the axis of the participation coefficient (see Figs. 2b and S7).

High reproducibility was also found for between-state differences in centroid edge weights across all runs in the HCP dataset (see Figs. 3b and S8). Both in the HCP and NKI datasets, decreased (respectively, increased) functional connectivity during the integrated state was observed within (respectively, between) task-negative and task-positive networks on average as we described in **Results**, while the decreased functional connectivity within task-positive networks was more pronounced within/between the SMN and VIS in the HCP dataset and within/between the DAN and VAN in the NKI dataset.

Reproducibility of between-state differences in structure-function relationships

Edge weights

Between-state differences in the relationship between structural and functional edge weights were reproducible across runs and datasets. In all runs of the HCP and NKI datasets, we observed elevated similarity of edge weights in the integrated state (Figs. 4a and S9a), a predominance of the DMN in the pair-wise between-state differences in the edge weight similarity (Figs. 4b and S9b) and greater between-state differences in the DMN–DAN than those assessed over the whole cortex (Figs. 4c and S9c). In the NKI dataset we also found large pair-wise between-state differences in the DAN together with the DMN. Pairs of network components from which between-state differences were found to be greater than those evaluated

over the whole cortex were not identical across runs and datasets, but the DMN–DAN was consistently such a pair of components in all runs of the HCP and NKI datasets (see Figs. 4c and S9c). There were also several minor differences between the datasets in, e.g., the overall magnitude of the edge weight similarity and the t-scores of the between-state differences; however, they did not compromise our three major findings listed above in this paragraph.

Partitions

We also confirmed a high reproducibility of between-state differences in the structure-function relationships of network partitions across runs and datasets. Elevated similarity of partitions in the integrated state (Figs. 5a and S10a) and increased within-functional-module density of direct structural connections in the integrated state (Figs. 5b and S10b) were observed throughout all runs of the HCP and NKI datasets. Increased within-functional-module density of indirect structural connections in the segregated state was found with the path length $L = 3$ in all runs and datasets (see Figs. 5b and S10b). Small between-state differences in the density of indirect connections with $L = 2$ was observed in run 2LR of the HCP dataset but it was not significant in all the other runs. We observed another minor difference between the datasets in the overall magnitude of the similarity of partitions, whereas the relative relationship between the segregated and integrated states in the similarity score was invariant across the two datasets.

Relations to head movements

To demonstrate that fluctuations between segregated and integrated states are not merely an artifact of the head movements, we examined in more detail the relationship between a network attribute for integration (the mean participation coefficient [mean $\boldsymbol{P}_t$]) and a measure of head motion (framewise displacement [FD]) in run 2LR of the HCP dataset. Figure S11a displays the time courses of mean $\boldsymbol{P}_t$ and FD in the three subjects whose Pearson correlation coefficient between mean $\boldsymbol{P}_t$ and the sliding-window-averaged FD was closest to the 5th percentile, the median and the 95th percentile, respectively, of the distribution of this correlation coefficient over subjects. As shown in this figure, peaks and dips of mean $\boldsymbol{P}_t$ and FD were not consistently related to each other, indicating no clear relation between these two time courses. In addition, the correlation coefficient between mean $\boldsymbol{P}_t$ and the sliding-window-averaged FD was neither consistently positive nor negative within each individual as seen in Fig. S11b; this correlation coefficient averaged across subjects was nearly zero (0.040). The time-lagged correlation coefficient was also very weak; the lagged correlation averaged over subjects ranged between 0.015 and 0.055 for time lags from -30 s to 30 s. Furthermore, mean $\boldsymbol{P}_t$ and FD, which were averaged over time, also had a low correlation coefficient (-0.015) across subjects (see Fig. S11c). Between-state differences in the sliding-window-averaged FD were also very small (segregated, 0.084 ± 0.026 [mean $\pm$ SD]; integrated, 0.085 ± 0.027; Cohen's $d = 0.048$). Altogether, these observations suggest that head motion did not compromise our findings of the segregated

and integrated states of functional connectivity.

Relations to other potential confounds

In addition to head movements, we further examined the relationships of fluctuations in network integration to other potential confounds, i.e. respiration and the strength and variability of global rs-fMRI signal, in run 2LR of the HCP dataset.

The respiratory signal was simultaneously recorded during the acquisition of rs-fMRI data in the HCP dataset (Van Essen et al. 2013; available for 70 subjects in our sample set [$n = 84$]). Log files containing this signal were downloaded after the HCP fixed an issue of timing errors in earlier versions. Other than taking sliding-window averages, the raw respiratory belt trace was used without further processing in our analysis as in Power et al. (2017). With this setting, we did not observe any clear relationships between mean $\boldsymbol{P}_t$ and the sliding-window-averaged respiratory belt trace. As seen in Fig. S12 left, the correlation coefficient between these two timeseries was neither consistently positive nor negative within each individual (its average across subjects was -0.022). Furthermore, the temporal mean of the sliding-window-averaged respiratory belt trace within each state did not differ significantly between the segregated and integrated states ($p = 0.26$).

Fluctuations in the strength and variability of global rs-fMRI signal were tracked with the sliding-window mean and SD, respectively, of regional rs-fMRI signals averaged over the whole cortex. We confirmed that neither positive nor negative correlations were consistently associated between mean $\boldsymbol{P}_t$ and these global timeseries (see Fig. S12 middle and right). Their correlation coefficients averaged across subjects were 4.2×10^{-3} (sliding-window mean) and -0.038 (sliding-window SD). Moreover, neither the temporal average of the sliding-window mean nor SD of global rs-fMRI signal within each state differed significantly between the segregated and integrated states (sliding-window mean, $p = 0.46$; sliding-window SD, $p = 0.61$).

These results support the notion that detected fluctuations in network integration are not merely due to changes in the timing of respiration or in the strength or variability of global rs-fMRI signal.

References

Ashburner J (2012) SPM: a history. NeuroImage 62:791–800

Betzel RF, Byrge L, He Y, Goñi J, Zuo XN, Sporns O (2014) Changes in structural and functional connectivity among resting-state networks across the human lifespan. NeuroImage 102:345–357

Betzel RF, Fukushima M, He Y, Zuo XN, Sporns O (2016) Dynamic fluctuations coincide with periods of high and low modularity in resting-state functional brain networks. NeuroImage 127:287–297

Cammoun L, Gigandet X, Meskaldji D, Thiran JP, Sporns O, Do KQ, Maeder P, Meuli R, Hagmann P (2012) Mapping the human connectome at multiple scales with diffusion spectrum MRI. J Neurosci Methods 203:386–397

Cox RW (2012) AFNI: what a long strange trip it's been. NeuroImage 62:743–747

Fischl B (2012) FreeSurfer. NeuroImage 62:774–781

Friston KJ, Williams S, Howard R, Frackowiak RS, Turner R (1996) Movement-related effects in fMRI time-series. Magn Reson Med 35:346–355

Jenkinson M, Beckmann CF, Behrens TEJ, Woolrich MW, Smith SM (2012) FSL. NeuroImage 62:782–790

Nooner KB, Colcombe SJ, Tobe RH, Mennes M, Benedict MM, Moreno AL, Panek LJ, Brown S, Zavitz ST, Li Q, Sikka S, Gutman D, Bangaru S, Schlachter RT, Kamiel SM, Anwar AR, Hinz CM, Kaplan MS, Rachlin AB, Adelsberg S, Cheung B, Khanuja R, Yan C, Craddock CC, Calhoun V, Courtney W, King M, Wood D, Cox CL, Kelly AMC, Di Martino A, Petkova E, Reiss PT, Duan N, Thomsen D, Biswal B, Coffey B, Hoptman MJ, Javitt DC, Pomara N, Sidtis JJ, Koplewicz HS, Castellanos FX, Leventhal BL, Milham MP (2012) The NKI-Rockland sample: a model for accelerating the pace of discovery science in psychiatry. Front Neurosci 6:152

Power JD, Plitt M, Laumann TO, Martin A (2017) Sources and implications of whole-brain fMRI signals in humans. NeuroImage 146:609–625

Tournier JD, Calamante F, Connelly A (2007) Robust determination of the fibre orientation distribution in diffusion MRI: non-negativity constrained super-resolved spherical deconvolution. NeuroImage 35:1459–1472

Tournier JD, Calamante F, Connelly A (2012) MRtrix: diffusion tractography in crossing fiber regions. Int J Imaging Syst Technol 22:53–66

Van Essen DC, Smith SM, Barch DM, Behrens TEJ, Yacoub E, Ugurbil K for the WU-Minn HCP Consortium (2013) The WU-Minn Human Connectome Project: an overview. NeuroImage 80:62–79

Xu T, Yang Z, Jiang L, Xing XX, Zuo XN (2015) A Connectome Computation System for discovery science of brain. Sci Bull 60:86–95

Yeo BTT, Krienen FM, Sepulcre J, Sabuncu MR, Lashkari D, Hollinshead M, Roffman JL, Smoller JW, Zollei L, Polimeni JR, Fischl B, Liu H, Buckner RL (2011) The organization of the human cerebral cortex estimated by intrinsic functional connectivity. J Neurophysiol 106:1125–1165

Yeo BTT, Tandi J, Chee MWL (2015) Functional connectivity during rested wakefulness predicts vulnerability to sleep deprivation. NeuroImage 111:147–158

Zalesky A, Fornito A, Cocchi L, Gollo LL, Breakspear M (2014) Time-resolved resting-state brain networks. Proc Natl Acad Sci U S A 111:10341–10346

Supplementary figures

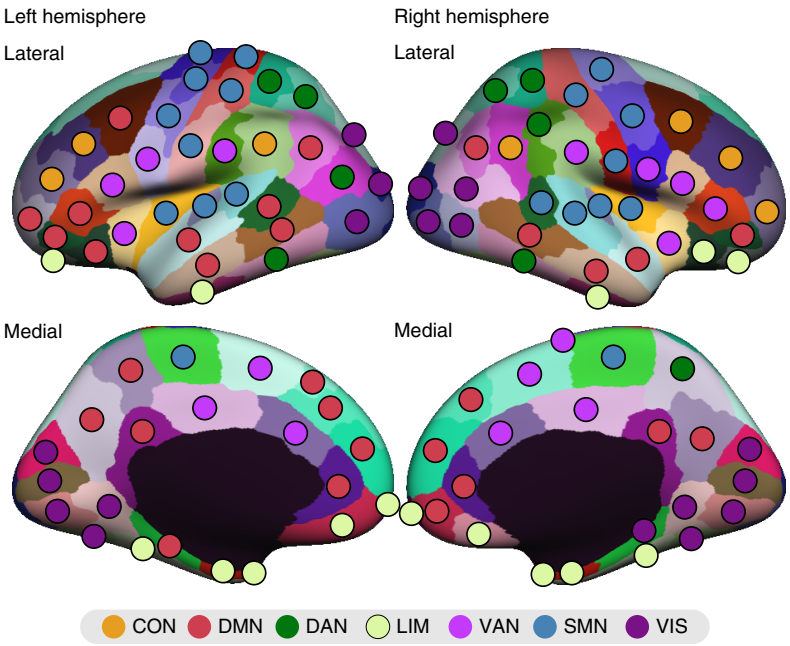

Fig. S1 Cortical parcellation employed in the HCP dataset. The 68 cortical parcels in the Desikan-Killiany atlas are subdivided into a total of 114 parcels (Cammoun et al. 2012). A colored circle in each cortical parcel indicates which network component of the 7-Network parcellation in Yeo et al. (2011) is maximally overlapped with the corresponding parcel

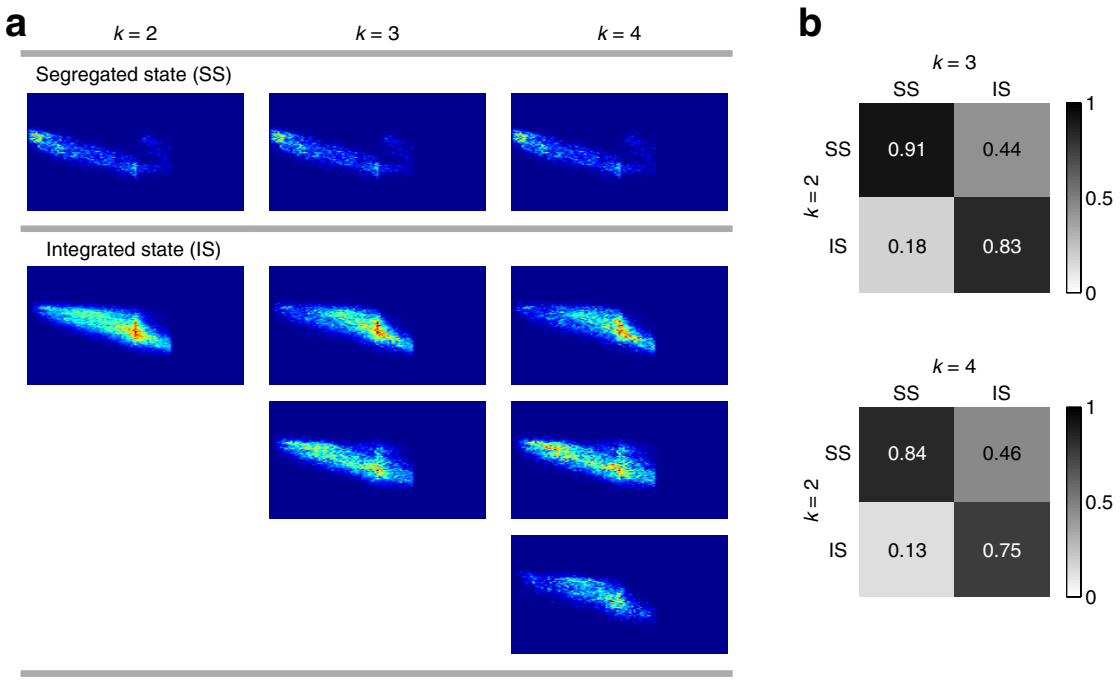

Fig. S2 a Joint histograms of the within-module degree z-score and the participation coefficient within each cluster for $k = 2$, 3 and 4 in a representative subject. In each k, one cluster with the lowest mean partition coefficient averaged across regions and time was associated with the segregated state. **b** Averaged similarity of the joint histograms within and between states (top: $k = 2$ vs. $k = 3$; bottom: $k = 2$ vs. $k = 4$). Similarity scores were averaged over all subjects. The similarity of joint histograms was quantified using the Pearson correlation coefficient

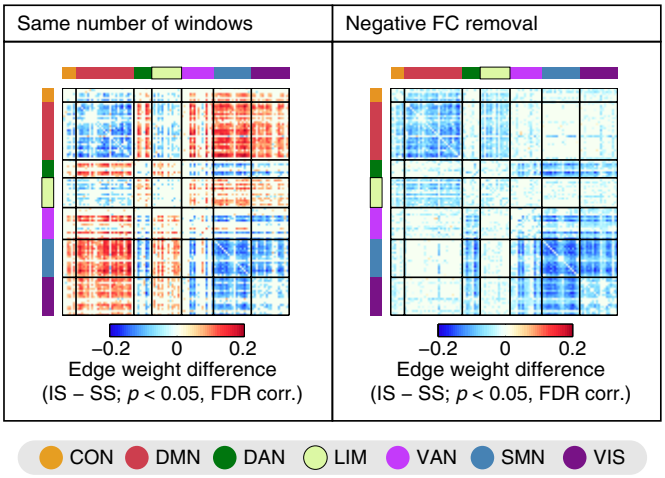

Fig. S3 Between-state differences in centroid edge weights with the same number of time windows across the states and the removal of negative functional connectivity (FC). For descriptions of each panel, see the caption of Fig. 3b

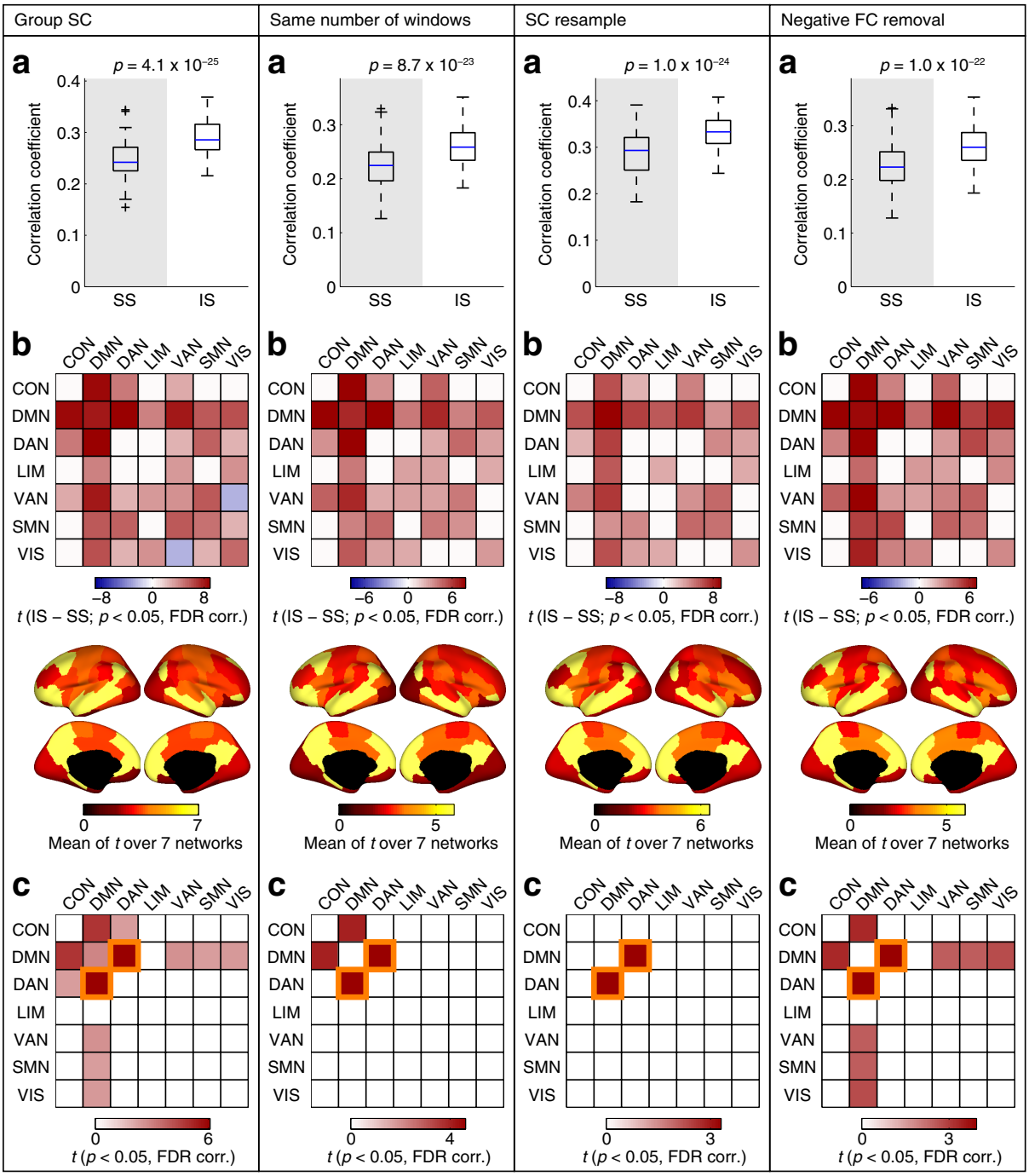

Fig. S4 Structure-function relationships of edge weights with group-level structural connectivity (SC), the same number of time windows across the states, the resampled SC and the removal of negative functional connectivity (FC). For descriptions of each panel, see the caption of Fig. 4

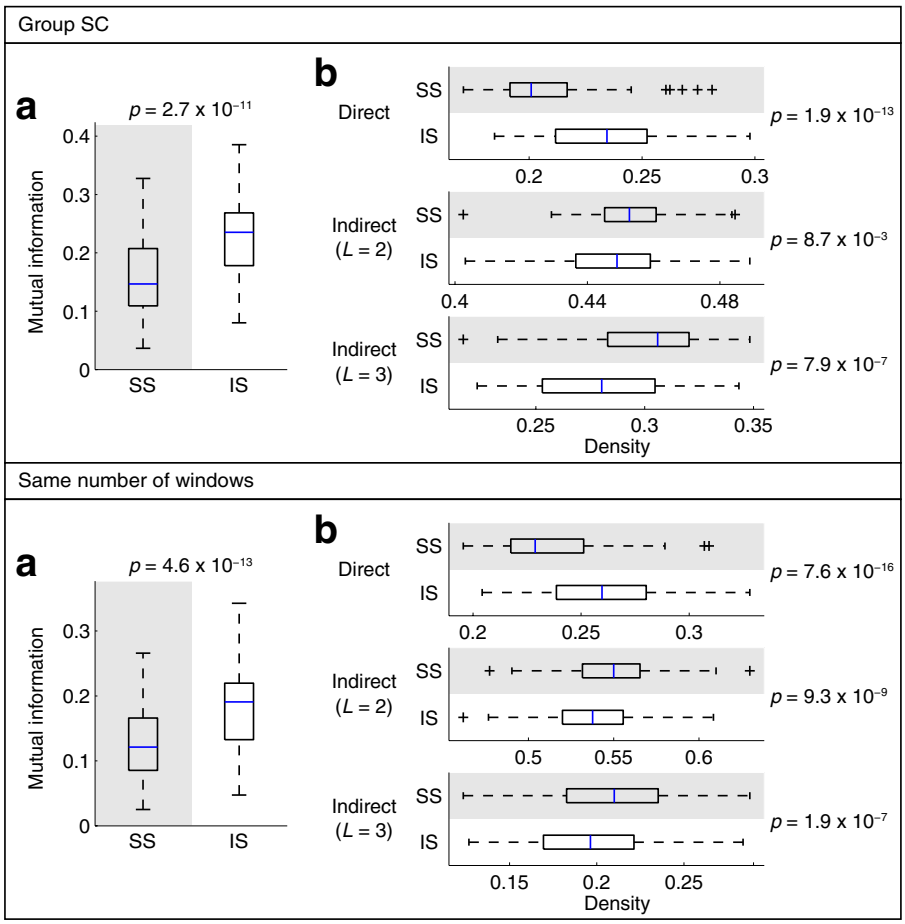

Fig. S5 Structure-function relationships of network partitions with group-level structural connectivity (SC) and the same number of time windows across the states. For descriptions of each panel, see the caption of Fig. 5

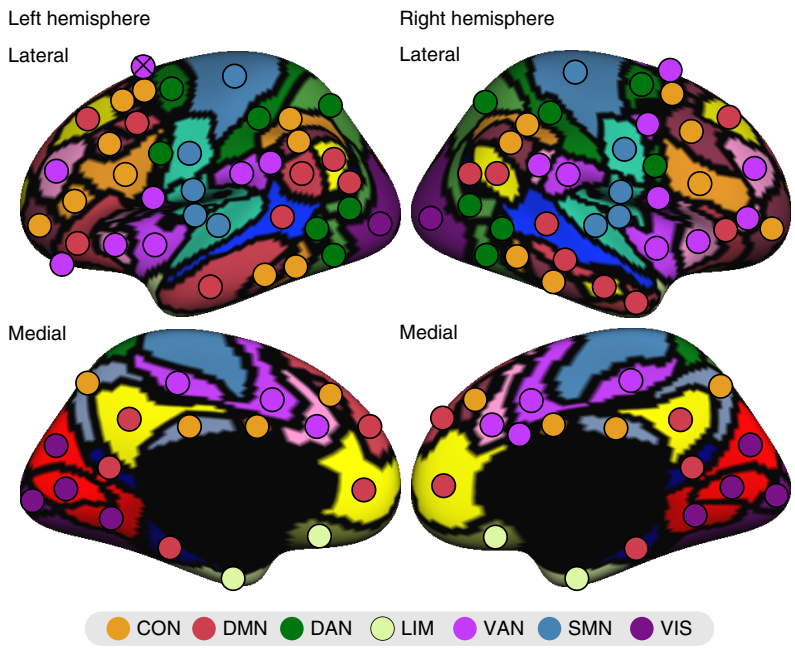

Fig. S6 Cortical parcellation employed in the NKI dataset. The 17 network components in Yeo et al. (2011) are subdivided into 114 regions (Betzel et al. 2014; Yeo et al. 2015). A colored circle in each parcel shows which network component of the 7-Network parcellation in Yeo et al. (2011) is maximally overlapped with the corresponding parcel. One parcel indicated by $\otimes$ in the top left surface map was discarded in this study because of its small surface area

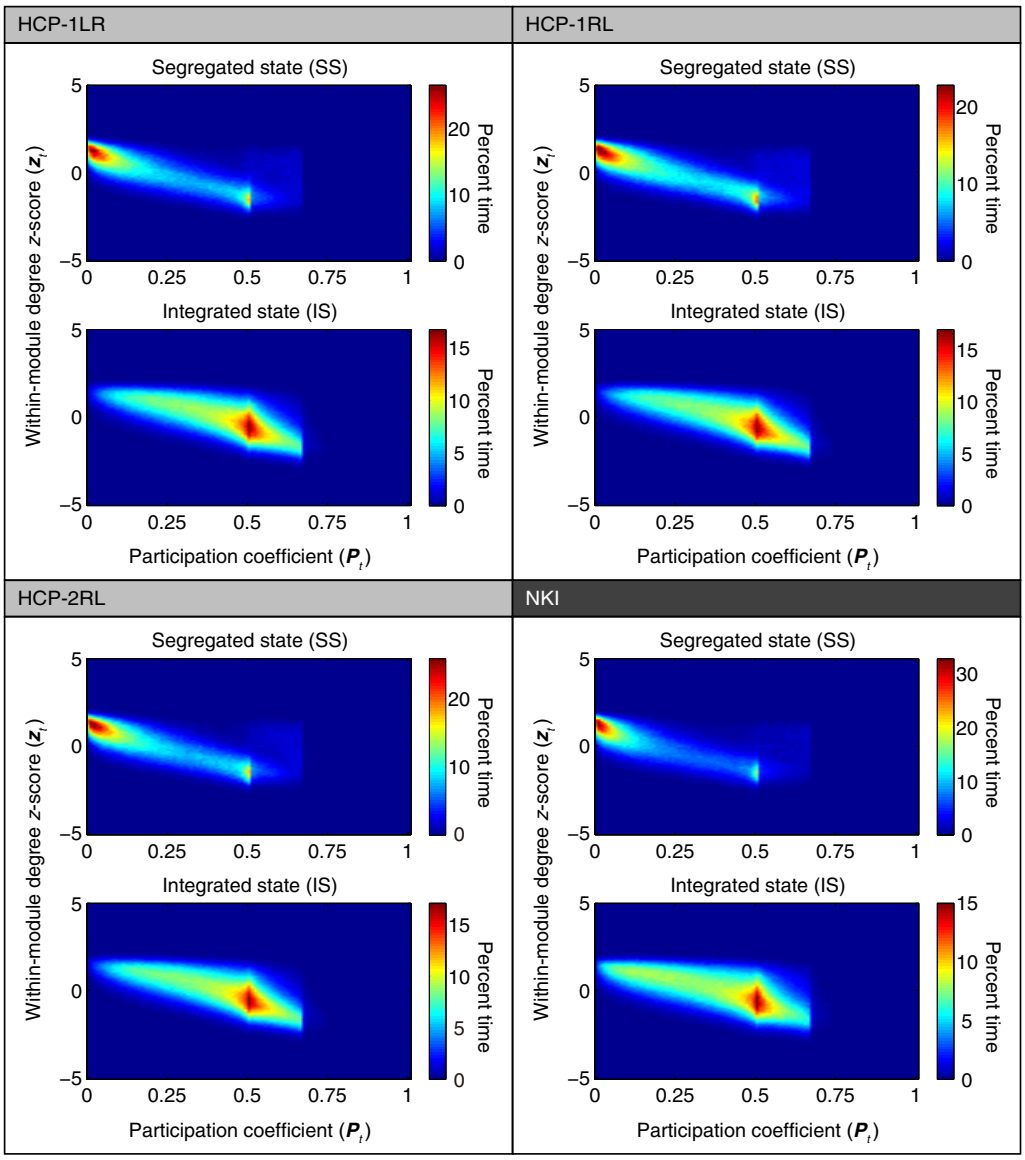

Fig. S7 Joint distributions of the within-module degree z-score and the participation coefficient in the other three runs (1LR, 1RL and 2RL) of the HCP dataset and a single run of the NKI dataset. For descriptions of each panel, see the caption of Fig. 2b

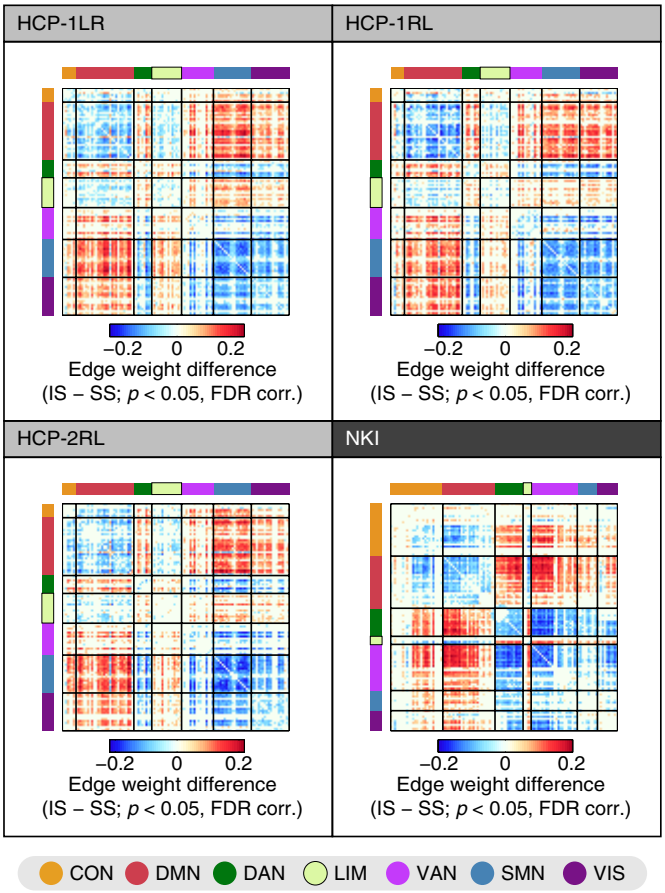

Fig. S8 Between-state differences in centroid edge weights in the other three runs (1LR, 1RL and 2RL) of the HCP dataset and a single run of the NKI dataset. For descriptions of each panel, see the caption of Fig. 3b

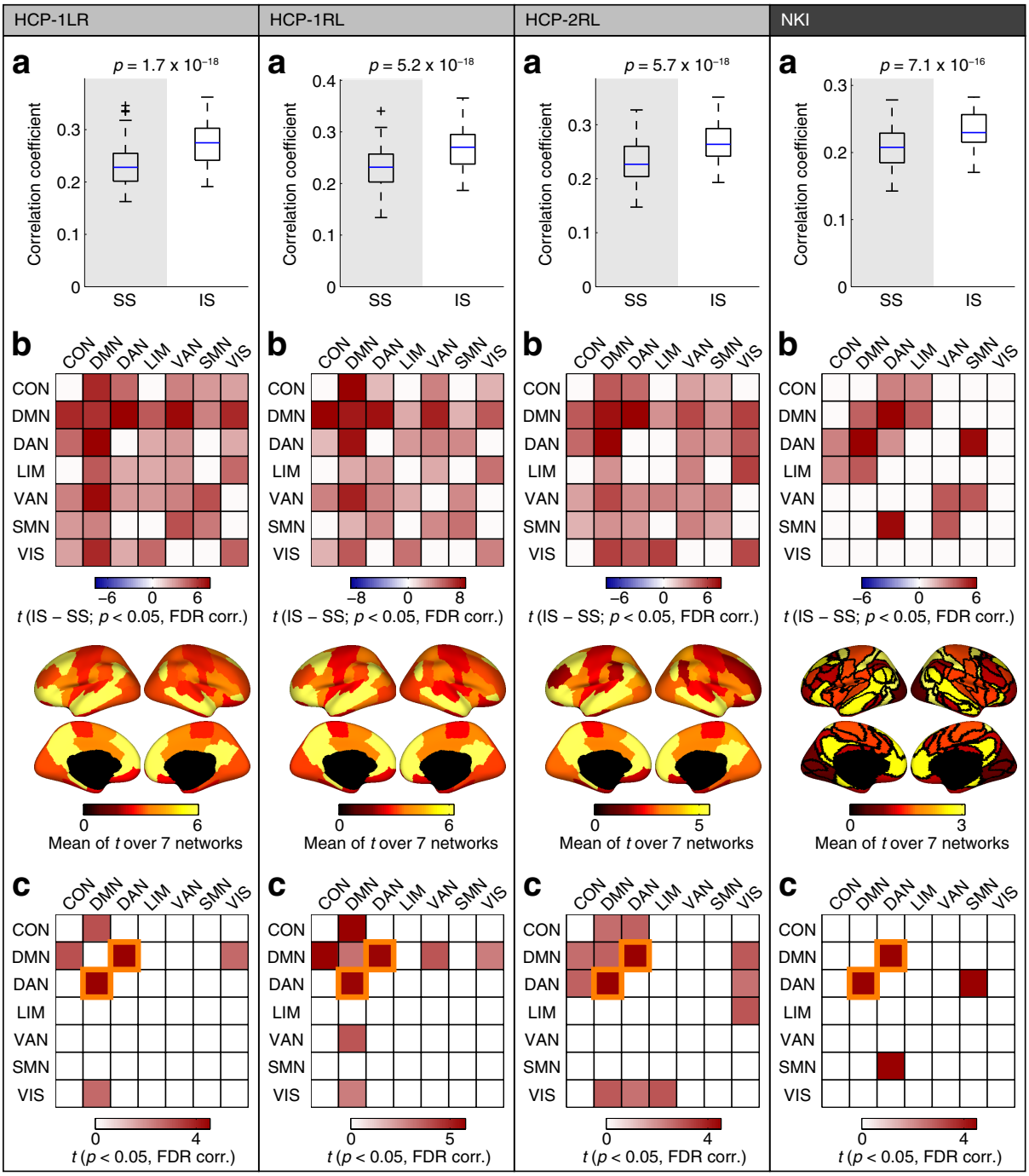

Fig. S9 Structure-function relationships of edge weights in the other three runs (1LR, 1RL and 2RL) of the HCP dataset and a single run of the NKI dataset. For descriptions of each panel, see the caption of Fig. 4

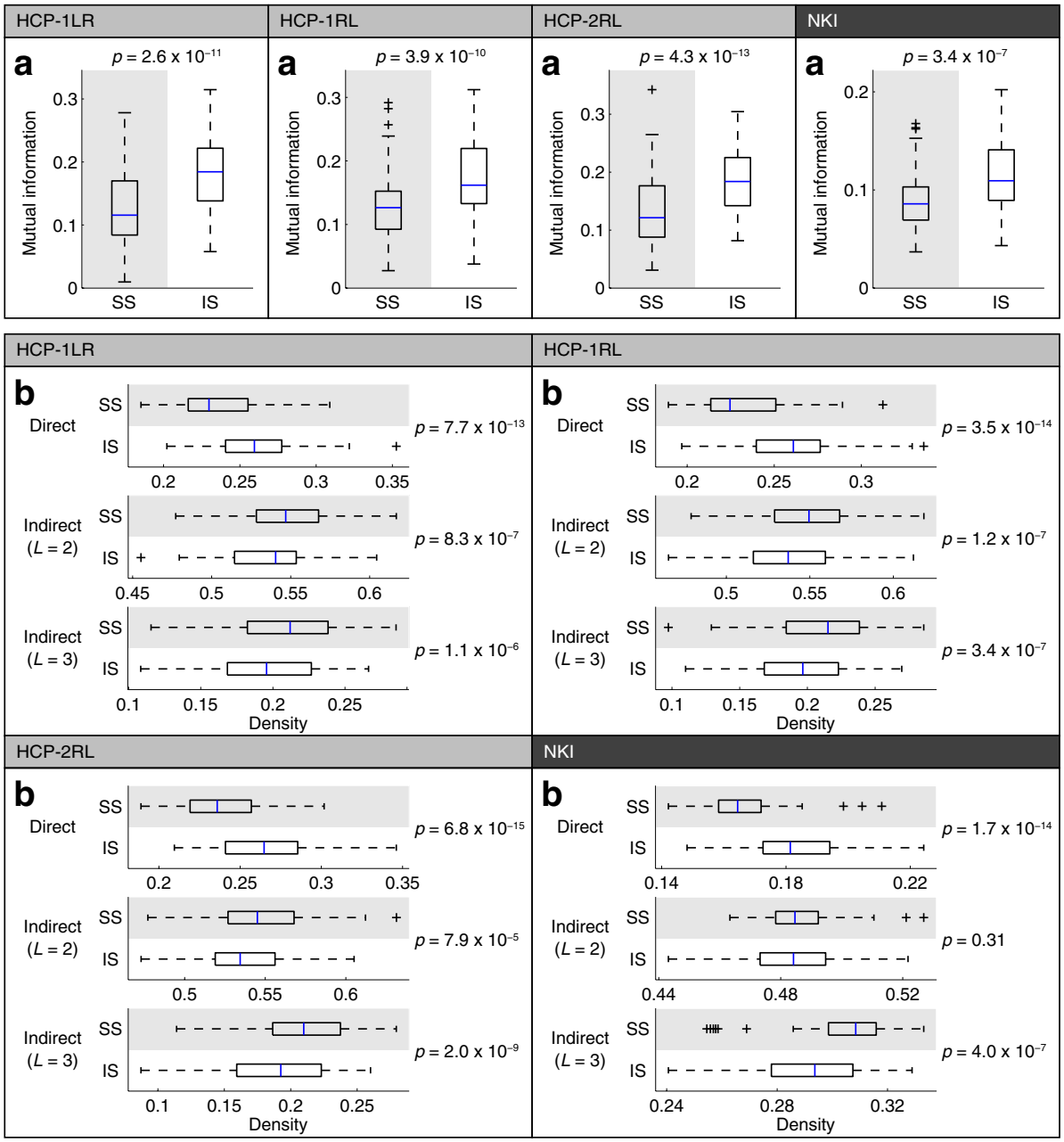

Fig. S10 Structure-function relationships of network partitions in the other three runs (1LR, 1RL and 2RL) of the HCP dataset and a single run of the NKI dataset. For descriptions of each panel, see the caption of Fig. 5

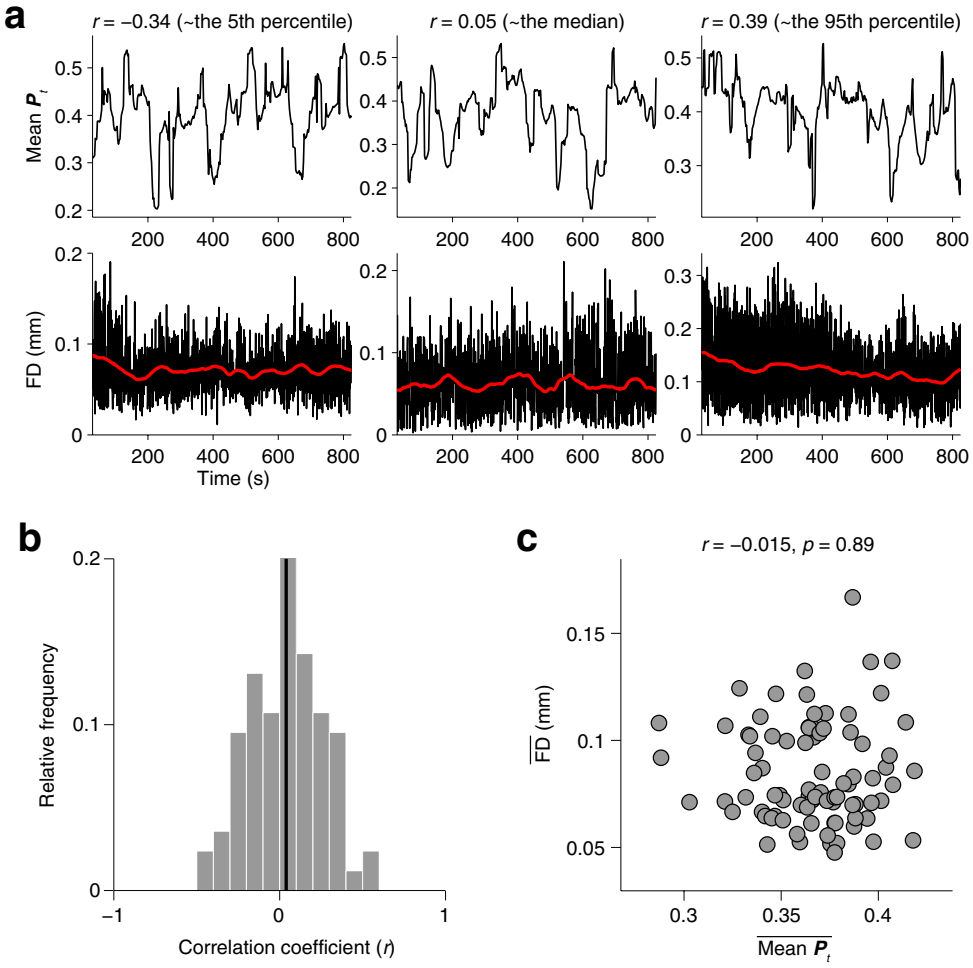

Fig. S11 Temporal fluctuations in network integration and head movement. **a** Upper: mean participation coefficient $\boldsymbol{P}_t$. Lower: framewise displacement (FD) (black) and its sliding window average (red). Here, we show mean $\boldsymbol{P}_t$ and FD in the three subjects whose Pearson correlation coefficient between mean $\boldsymbol{P}_t$ and the sliding-window-averaged FD was closest to the 5th percentile, the median and the 95th percentile, respectively, of the distribution of this correlation coefficient over subjects. **b** A histogram showing the distribution of the correlation coefficient between mean $\boldsymbol{P}_t$ and the sliding-window-averaged FD. The vertical line near zero indicates the mean across subjects. **c** A scatter plot of mean $\boldsymbol{P}_t$ and FD that were averaged over time

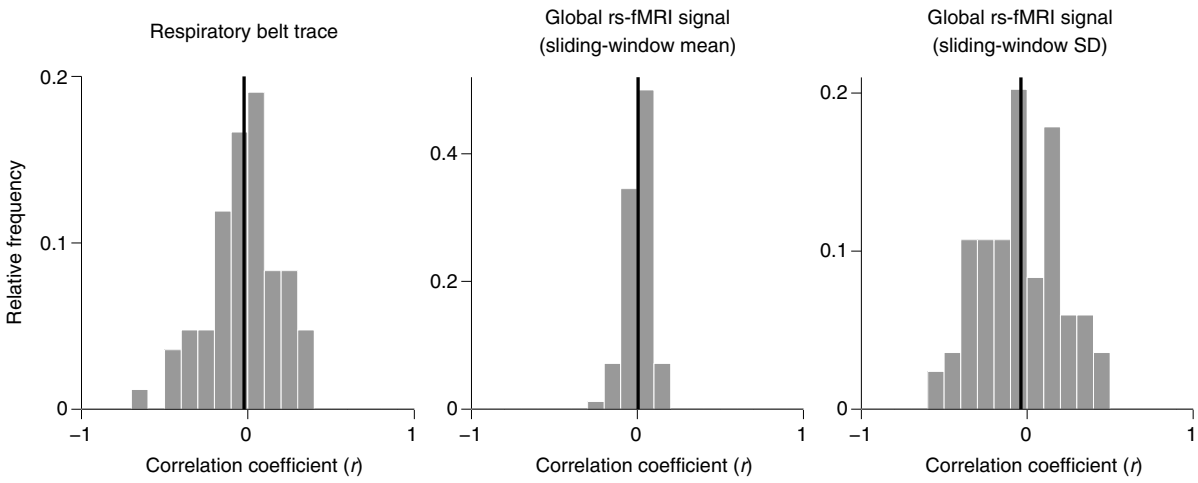

Fig. S12 Left: the distribution of the correlation coefficient between mean $\boldsymbol{P}_t$ and the sliding-window-averaged respiratory belt trace. Middle/Right: the distribution of the correlation coefficient between mean $\boldsymbol{P}_t$ and the strength (middle) or the variability (right) of global rs-fMRI signal. The vertical line near zero in each histogram indicates the mean across subjects